A 3D multi-scale skeletal muscle model to predict active and passive responses. Application to intra-abdominal pressure prediction

Mina Karami[a], Hassan Zohoor[b,c], Begoña Calvo[d,e], Jorge Grasa[d,e,*]

[a] *School of Mechanical Engineering, Sharif University of Technology, Azadi Ave., Tehran, Iran*
[b] *Center of Excellence in Design, Robotics and Automation, Sharif University of Technology, Azadi Ave., Tehran, Iran*
[c] *The Academy of Sciences of IR Iran, Haqqani HWY, Tehran, Iran*
[d] *Aragón Institute of Engineering Research (I3A), Universidad de Zaragoza, Zaragoza, Spain*
[e] *CIBER-BBN Centro de Investigación en Red en bioingeniería, Biomateriales y Nanomedicina, Universidad de Zaragoza, Zaragoza, Spain*

Abstract

Computational models have been used extensively to study the behavior of skeletal muscle structures, however few of these models are able to evaluate their 3D active response using as input experimental measurements such as electromyography. Hence, improving the activation mechanisms in simulation models can provide interesting and useful achievements in this field. Therefore, the purpose of this paper was to develop a multi-scale chemo-mechanical material model to consider the active behavior of skeletal muscle in 3D geometries. The model was used to investigate the response of abdominal muscles which represent a challenging scenario due to their complex geometry and anatomical conditions. Realistic muscle geometries and other tissues of the human abdomen, including transverse abdominis (TA), internal oblique (IO), external oblique (EO), rectus abdominis (RA), rectus sheath (RSH), linea alba (LA) and aponeurosis (APO) were considered. Since the geometry of these tissues was obtained from magnetic resonance images, an iterative algorithm was implemented to find the initial stress state that achieve the equilibrium of them with the intra-abdominal pressure. In order to investigate the functionality of the proposed model, the increase of intra-abdominal pressure was calculated during cough in the supine position while the Ca^{2+} signal for activating the muscles was set in regard to experimentally recorded electrical activity from previous studies. The amount of intra-abdominal pressure calculated by the model is consistent with reported experimental results. This model can serve as a virtual laboratory to analyze the role of the abdominal wall components in different conditions, such as the performance of meshes used for repairing hernia defects.

1. Introduction

The human abdominal wall surrounding the abdominal cavity has a complex geometry that can be assumed as a composite structure with different stacked layers. The anterolateral part of this structure comprises layers of skeletal muscle (rectus abdominis RA, transverse abdominis TA, external oblique EO, and internal oblique

---

* Corresponding author at: Aragón Institute of Engineering Research (I3A), Universidad de Zaragoza, Zaragoza, Spain.
 E-mail address: jgrasa@unizar.es (J. Grasa).

IO) and connective tissues (linea alba LA, rectus sheath RSH and aponeurosis APO) [1,2]. In addition to the musculoskeletal role of the wall in the upper body stability and assistance in breathing, it protects the internal organs against trauma and intends to withstand internal abdominal pressure (IAP) during different postures. The interaction between these tissues and organs along with the common hernia problem represents a great need for research in this area [3,4]. In cases of trauma, high IAP can have severe negative consequences. These may include a decrease in cardiac output due to decreased venous return, a decrease in perfusion of the liver and other organs, as well as reduced blood flow to the kidneys and a subsequent reduction in glomerular filtration rate [5]. Additionally, understanding the biomechanics of the abdominal wall can be important in the development of biomaterials and other surgical interventions used in the repair of abdominal wall defects [6,7]. The coupling between the mechanical and chemical processes during the excitation-contraction is also important to consider in an accurate representation of the real-life performance of the muscle. By modeling these aspects, researchers can gain a better understanding of the underlying mechanisms driving muscle contraction and identify potential targets for therapeutic intervention, developing effective treatments for disorders such as muscular dystrophy or a better understanding of muscle fatigue [8].

Several studies have attempted to identify the characteristics of the abdominal wall by experimenting on human and different animal specimens (rat, rabbit, dog and pig). However, empirical data on human samples are limited. The mechanical behavior of connective tissues in the abdomen has been analyzed with different methods such as uniaxial, biaxial, or burst strength tests [9–12]. The work of Cardoso et al. [13] is a unique study that investigated the passive behavior of individual layers of abdominal muscles from cadaveric human samples. In this study, the stress–stretch relationships of EO, IO, TA, and RA were reported according to the uniaxial tensile test along the main fibers of the muscle. Empirical results demonstrated that abdominal wall tissues have highly anisotropic and complicated behavior due to the presence of muscle and collagen fibers [9,14,15].

Since active behavior of muscles cannot be investigated using cadaveric specimens, there are only few experimental data available for some important characteristics such as the active force dependence with the muscle length and the force-stimulation frequency relationships. This information could only be found for some of the abdominal wall muscles of canine [16,17], hamster [18], and rabbit [19].

In the whole body, however, the components of the abdominal wall act as an integrated composite structure so that its functional characteristics can be different from those of the individual layers. The experimental results of Hernández et al. [20] substantiated this fact when a multilayer sample of abdominal wall exhibits less anisotropic behavior than its individual layers.

As a result, some researchers used the ex vivo approach to study the behavior of intact abdominal wall subjected to different intra-abdominal pressure (IAP) [21–24]. Accuracy of the cadaveric experimental results may be reduced because of some problems such as using frozen samples, long sample preparation which causes dehydration, and elimination of initial strain due to cutting the wall tissue.

Another group of studies developed non-invasive in vivo approaches for the investigation of intact abdominal wall behavior [25–29]. The effect of muscular contraction was considered in these approaches, except in those that were performed on anesthetized subjects [30–32].

Although the experimental studies provide invaluable information about the biomechanical properties of tissues, there are quite many barriers to overcome, such as high time and cost consumption, the limited number of cases, unavailable to cover the geometrical complexities when the type of layers vary with position, active behavior obstacles and ethics aspects of research. In this regard, there is always a tendency to use simulation as an efficient and complementary tool in biomechanics research.

Hernández et al. [20] determined experimentally the mechanical properties of individual layers of the rabbit abdominal wall and simulated an ideal geometry of this region by considering a hyperelastic anisotropic material model. They continued abdominal wall investigation on a realistic geometry of human full torso against different intra-abdominal pressure [33]. In these studies, only passive behavior of the abdominal muscles were considered.

Pachera et al. [34] provided an integrated real geometry of the human abdominal wall and implemented a hyperelastic and almost incompressible material model, which considered the effect of fiber directions as well. They simulated the abdominal wall behavior under three intra-abdominal pressure levels when only the passive behavior of the muscles was considered. In a subsequent study, active muscle response was added to the material model in the form of a three-element Hill model [35]. Their results demonstrated that displacement of the abdominal wall is decreased by considering active behavior into account. They used laser scanning to record the antero-lateral

abdominal wall surface in both the relaxed and abdominal muscles contraction posture [29]. Subsequently, they developed the 3D geometry to model each muscle separately [36]. In that study, abdominal wall displacement was simulated while all the muscles were equally activated. The displacement results of the simulation were compared with the experimental data recorded in a previous study [29]. Moreover, there are multiple numerical studies that investigate the likeliness of hernia formation and suitable surgical mesh types and features [3,4,7,33,37,38]. All of these researches only considered the passive response of the muscles in the simulation.

Due to the great challenges of experimental and numerical investigations about the active behavior of the abdominal wall muscles, just a few studies have been conducted in this regard. However, hernia abnormality is directly related to the weakness of muscles. Therefore, considering the active behavior of the muscles along with their passive reaction will play an important role in the accuracy of the extracted results [6,39].

The aim of this study is to investigate the behavior of human abdominal wall with a new material model that allows for activation of the muscles through changes in the intracellular calcium ion concentration. Unlike previous models [40,41] that accounts for force generation in a way to reduce energy consumption, termed the latch state that is a unique ability of smooth muscle, the present model considers the effect of the regulatory complex troponin-tropomyosin, specifically for skeletal muscle. Therefore, the chemical kinetics in the model stablish a set of states that account for transducing the effect of calcium on contractile protein activation and also for inhibiting actin and myosin interaction. This new material formulation allows for activating each muscle separately and in proportion to available experimental EMG data. In this way, the operation of the 3D muscle model is connected in a more realistic way with the physiological process of activation. Traditionally, existing skeletal muscle models triggered the activation by a certain parameter or activation function [19,35,36,42]. Furthermore, the initial strains of the tissue are taking into account for providing more realistic results during the simulation of cough in a supine position.

In the next section, the 3D constitutive relations of a chemo-mechanical material model for muscles are presented. In Section 3, material model is specialized for the abdominal wall and its real 3D geometry has been prepared with considering the initial strains. In Section 4, estimated results for the intra-abdominal pressure and related displacement and stress contours are reported. In Section 5, validation of the results and relationships between variables of the model are discussed.

2. Constitutive material model

This study presents a chemo-mechanical material model for skeletal muscles that appropriately control muscles' active behavior in 3D. To that end, the one-dimensional chemo-mechanical model for skeletal muscle contraction by Karami et al. [8] is extended to three dimensions.

2.1. Chemical kinetics

In any way that skeletal muscle is stimulated, the release of calcium ion from the sarcoplasmic reticulum (SR) into the intracellular environment will trigger cross-bridge kinetics and subsequently, force generation [43]. This model consists of four states between actin and myosin in cross-bridge cycle (Fig. 1). At the R_{off} state actin and myosin are detached as the actin-binding site is covered by the regulatory complex. As the concentration of Ca^{2+} increases, the regulatory unit unbinds the myosin sites (D state) but the cross-bridge is not yet formed. The attachment occurs in the A_1 state (weak) that represent the pre-power stroke and at the A_2 state (strong) or post-power stroke.

Switching between R_{off} and D states is controlled by two calcium-dependent rates k^{off} and k^{on}:

$$k^{\text{off}} = k_0^{\text{off}} + \left(k_{\text{Ca}}^{\text{off}} - k_0^{\text{off}}\right) \left(\left[Ca^{2+}\right]^p / \left(\left[Ca_{50}^{2+}\right]^p + \left[Ca^{2+}\right]^p\right)\right) \tag{1}$$

$$k^{\text{on}} = k_0^{\text{on}} + \left(k_{\text{Ca}}^{\text{on}} - k_0^{\text{on}}\right) \left(\left[Ca^{2+}\right]^p / \left(\left[Ca_{50}^{2+}\right]^p + \left[Ca^{2+}\right]^p\right)\right) \tag{2}$$

where $k_{\text{Ca}}^{\text{off}}$ and k_0^{off} are rate constants changing the regulatory complex to the off situation, with and without the presence of Ca^{2+}, respectively; and $k_{\text{Ca}}^{\text{on}}$ and k_0^{on} are equivalent constants when moving to the D state. For the generation of 50% maximum force in muscle, the concentration of Ca^{2+} needs to reach $[Ca_{50}^{2+}]$. The transition among other states (D, A_1 and A_2) is governed by the other five constant rate coefficients (f, f', h, h' and g).

The hierarchical structure of the skeletal muscle allows for generalizing the behavior of individual muscle fibers and to extend it to the whole muscle response. Therefore, any state can be considered as a fraction of the probability
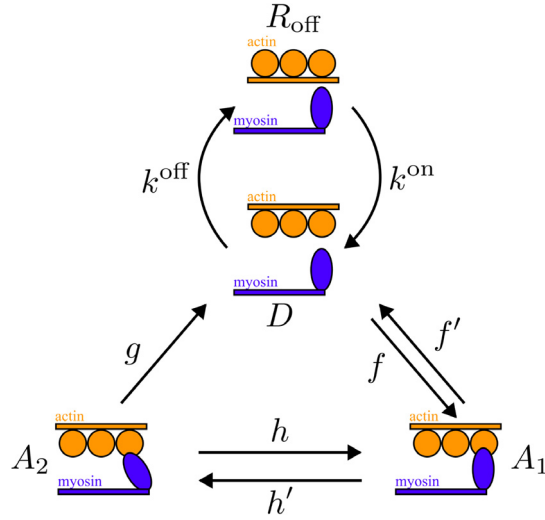
Fig. 1. Cross-bridge cycling model: off-regulatory unit (R_{off}), detached cross-bridge (D), Attached cross-bridge in pre (A_1) and post (A_2) power stroke [8].

that some cross-bridges of the muscle are in this situation. To that end, the following equation must be established among the states:

$$R_{\text{off}}(t) + D(t) + A_1(t) + A_2(t) = 1 \tag{3}$$

Furthermore, the probability of each chemical state at any given time can be calculated by the following ordinary differential equations [8]:

$$\frac{d}{dt}\begin{bmatrix} D \\ A_1 \\ A_2 \end{bmatrix} = \begin{bmatrix} -(k^{\text{on}} + k^{\text{off}} + f) & (f' - k^{\text{on}}) & (g - k^{\text{on}}) \\ f & -(f' + h) & h' \\ 0 & h & -(h' + g) \end{bmatrix}\begin{bmatrix} D \\ A_1 \\ A_2 \end{bmatrix} + \begin{bmatrix} k^{\text{on}} \\ 0 \\ 0 \end{bmatrix} \tag{4}$$

The slow or fast behavior of muscle fiber is affected by the speed of its cross-bridge cycle [44]. Therefore, proper selection of the chemical kinematic rate coefficients can model the overall behavior of the muscle in terms of fast or slow [45].

2.2. Kinematics

Considering Ω_0 is an initial configuration of a solid in the three-dimensional Euclidean space, see Fig. 2. Bijective time-dependent function β controls the motion of any point $X \in \Omega_0$ as:

$$\phi : \Omega_0 \times \mathbb{R} \to \Omega \tag{5}$$

Due to motion ϕ at time t, X positions to $x = x(X, t)$ and forms Ω that is called the current configuration.

$F = \partial x / \partial X$ is taken as the deformation gradient resulted from motion β. A common technique to take straightforwardly the quasi-incompressible behavior of the soft tissues ($J \approx 1$) into account is the multiplicative decomposition of F into a volumetric $(J^{1/3}I)$ and an isochoric part $(\bar{F})$ [46]:

$$F = \left(J^{1/3}I\right)\bar{F}, \qquad \bar{F} = J^{-1/3}F \tag{6}$$

$\bar{F}$ is known as the modified deformation gradient, $J = \det F > 0$ and I is the second-order identity tensor. Subsequently, the right and left Cauchy–Green deformation tensors and their modified equivalents can be defined, respectively as:

$$C = F^T F, \quad \bar{C} = \bar{F}^T \bar{F} = J^{-2/3}C \tag{7}$$

$$b = F F^T, \quad \bar{b} = \bar{F}\bar{F}^T = J^{-2/3}b \tag{8}$$
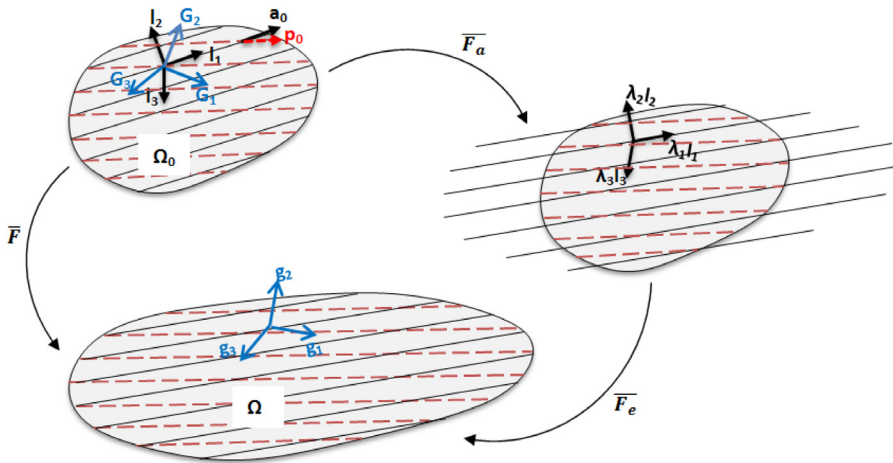
Fig. 2. Schematic view of initial configuration Ω_0 and two material anisotropic directions $\boldsymbol{a}_0\,(X)$, active behavior (contractile cells), and $\boldsymbol{p}_0(X)$, passive behavior (collagen fibers), at any point $X \in \Omega_0$. $\boldsymbol{G}_i$ is the reference global cartesian coordinate system. $\boldsymbol{L}_i = (\boldsymbol{l}_1, \boldsymbol{l}_2, \boldsymbol{l}_3)$ is the local rectangular coordinate system as $\boldsymbol{l}_1$ is aligned to active direction $\boldsymbol{a_0}$. Through the independent active contraction $\bar{\boldsymbol{F}}_a$ of muscular fibers, cartesian basis vectors ($\boldsymbol{L}_i$) deform to $\lambda_i \boldsymbol{L}_i$. Following the deformation of the elastic part $\bar{\boldsymbol{F}}_e$, the continuum maintains its integrity and transfer to current configuration Ω.

Similar to the kinematic assumption in [8], deformation of skeletal muscle activity is divided into two fictitious separate steps: first, deformation with regard to shortening behavior of myosin and actin, second, elastic deformation of cross-bridge to preserve the integrity of muscle (Fig. 2). Thus, modified deformation gradient can be multiplicatively decomposed as:

$$\bar{\boldsymbol{F}} = \bar{\boldsymbol{F}}_e \bar{\boldsymbol{F}}_a \tag{9}$$

In this equation $\bar{\boldsymbol{F}}_a$ is modeling the independent deformation of active filaments in Ω_0, and there is no need to be integrable. Thus, the middle configuration may not be compatible. $\bar{\boldsymbol{F}}_e$ which represents the elastic deformation in the muscle, will be formed to guarantee the compatibility of the final configuration in Ω (Fig. 2). Then, $\bar{\boldsymbol{C}}_e$ is defined as $\bar{\boldsymbol{C}}_e = \bar{\boldsymbol{F}}_e^T \bar{\boldsymbol{F}}_e = \bar{\boldsymbol{F}}_a^{-T} \bar{\boldsymbol{C}} \bar{\boldsymbol{F}}_a^{-1}$. $\bar{\boldsymbol{C}}_e$ depends on $\bar{\boldsymbol{F}}$ and $\bar{\boldsymbol{F}}_a$ and is not a state variable. Nevertheless, $\bar{\boldsymbol{C}}_e$ will be used in the following equations since it provides a convenient way for measuring elastic deformation.

Contractile proteins (actin and myosin) in skeletal muscles are aligned in a specific direction and organizes giving the characteristic striated configuration at the microscope. It is supposed that active contraction occurs along these lines and causes material anisotropy. Accordingly, two family of fibers are considered in the model to distinguish between muscular and collagen fibers. Although later the model is particularized for coincident directions of both fiber sets, this general formulation could be used for specific applications like muscle damage [47]. Thus for any point $X \in \Omega_0$, two distinct unite vectors $\boldsymbol{a}_0\,(X)$ and $\boldsymbol{p}_0\,(X)$ are considered as the anisotropic directions for active and passive mechanical behavior, respectively.

A set of local rectangular coordinate system $\boldsymbol{L}_i$ with the Cartesian basis vectors ($\boldsymbol{l}_1, \boldsymbol{l}_2, \boldsymbol{l}_3$) is defined in the tangent space Ω_0 so that $\boldsymbol{l}_1$ is aligned to active direction $\boldsymbol{a}_0$, $\boldsymbol{l}_2$ is perpendicular to $\boldsymbol{l}_1$ in the plane spanned by $\boldsymbol{a}_0$ and $\boldsymbol{p}_0$ ($\boldsymbol{l}_1 \cdot \boldsymbol{l}_2 = 0$) and $\boldsymbol{l}_3$ can be found by the right-handed cross product of $\boldsymbol{l}_1$ and $\boldsymbol{l}_2$ ($\boldsymbol{l}_1 \times \boldsymbol{l}_2 = \boldsymbol{l}_3$).

If assuming muscle just contracts along its active fibers $\boldsymbol{a}_0$, local active deformation gradient can be easily defined as:

$$\bar{\boldsymbol{F}}_a^{'} = \lambda_a \boldsymbol{l}_1 \otimes \boldsymbol{l}_1 + \lambda_a^{-1/2} \boldsymbol{l}_2 \otimes \boldsymbol{l}_2 + \lambda_a^{-1/2} \boldsymbol{l}_3 \otimes \boldsymbol{l}_3 \tag{10}$$

where λ_a is the magnitude of the contraction along the muscular fibers and a volume preserving condition is made for simplicity along perpendicular directions.

In the tangent space Ω_0, $\boldsymbol{G}_i$ is considered as the global cartesian coordinate system. The global contractile tensor can be found by means of the transformation tensor $\boldsymbol{Q}_{ij} = \boldsymbol{G}_i \cdot \boldsymbol{L}_j$:

$$\bar{\boldsymbol{F}}_a = \boldsymbol{Q}^T \bar{\boldsymbol{F}}_a^{'} \boldsymbol{Q} \tag{11}$$

Using the chain rule to take the time derivative of $\bar{\boldsymbol{F}}_a$ in Eq. (11) will provide a relation for calculating the contraction velocity of skeletal muscle fibers ($\dot{\lambda}_a$):

$$\dot{\bar{\boldsymbol{F}}}_a = \boldsymbol{Q}^T \frac{\partial \bar{\boldsymbol{F}}_a^{'}}{\partial \lambda_a} \dot{\lambda}_a \boldsymbol{Q} \tag{12}$$

with:

$$\frac{\partial \bar{\boldsymbol{F}}_a^{'}}{\partial \lambda_a} = \boldsymbol{l}_1 \otimes \boldsymbol{l}_1 - \frac{1}{2}\lambda_a^{-3/2}\boldsymbol{l}_2 \otimes \boldsymbol{l}_2 - \frac{1}{2}\lambda_a^{-3/2}\boldsymbol{l}_3 \otimes \boldsymbol{l}_3 \tag{13}$$

2.3. Balance laws

The principle of virtual power allows for deriving the balance laws of a continuum [48]. Accordingly, the following relation should be satisfied between the external $\left(\hat{P}_e\right)$ and internal power production $\left(\hat{P}_i\right)$ of the model in quasi-static conditions:

$$\hat{P}_i(\boldsymbol{\Gamma}, \eta, \mathcal{B}) + \hat{P}_e(\boldsymbol{\Gamma}, \eta, \mathcal{B}) = 0 \tag{14}$$

where $\boldsymbol{\Gamma}$, η, and $\mathcal{B}$ are fluxes associated with a set of admissible state variable velocities, contraction rates along the muscle fibers and fluxes of Ca^{2+} [41], respectively. The internal and external virtual power production can be defined as:

$$\hat{P}_i = -\int_{\Omega_0} \boldsymbol{P} : \nabla \boldsymbol{\Gamma} dV - \int_{\Omega_0} P_a \eta dV - \int_{\Omega_0} P_c \mathcal{B} dV \tag{15}$$

$$\hat{P}_e = \int_{\partial\Omega_0} \boldsymbol{T} \cdot \boldsymbol{\Gamma} ds - \int_{\Omega_0} T_a \eta dV - \int_{\Omega_0} T_c \mathcal{B} dV \tag{16}$$

where : represents double contraction, $\cdot$ denotes dot product, and ∇ is the material gradient. $\boldsymbol{P}$ is a first Piola–Kirchhoff stress tensor, $\boldsymbol{T}$ is the material traction vector. P_a and T_a are the internal and external thermodynamic forces associated to the contraction in the muscle fiber direction, respectively. These forces power-conjugate with η. P_c and T_c are the internal and external driving forces associated to the chemical potential that power-conjugate with $\mathcal{B}$. Equilibrium equations can be obtained by substituting Eqs. (16) and (15) in Eq. (14) and applying the divergence theorem:

$$\nabla \cdot \boldsymbol{P} = \boldsymbol{0} \quad in \quad \Omega_0, \qquad \boldsymbol{T} = \boldsymbol{P}^T \boldsymbol{N} \quad on \quad \partial\Omega_0 \tag{17}$$

$$P_a = T_a \quad in \quad \Omega_0, \qquad P_c = T_c \quad in \quad \Omega_0 \tag{18}$$

where $\boldsymbol{N}$ indicates a unit vector normal to the boundary $\partial\Omega_0$ of the initial configuration. P_a is interpreted as the active stress generated by the skeletal muscle fibers and P_c is assumed as a chemical potential carrying calcium ion current.

2.4. 3D hyperelastic constitutive equations

The second law of thermodynamics in the form of Clausius–Planck inequality by ignoring thermal effects can be written as [46]:

$$\dot{\psi} \leq \boldsymbol{P} : \dot{\boldsymbol{F}} + P_a \dot{\lambda}_a + P_c \dot{\beta} \tag{19}$$

The mechanical behavior of soft tissues such as skeletal muscles is considered hyperelastic, fiber-reinforced, and quasi-incompressible [8,42]. Therefore, a suitable free strain energy of skeletal muscle which can model its chemo-mechanical response, should depend on state variables $\left(\boldsymbol{F}, \lambda_a, \beta = \left[\text{Ca}^{2+}\right]\right)$, internal variables (chemical states), and active and passive anisotropic directions ($\mathcal{A} = \boldsymbol{a}_0 \times \boldsymbol{a}_0$ and $\mathcal{P} = \boldsymbol{p}_0 \times \boldsymbol{p}_0$) [8,41]. However, for modeling the elastic deformation of cross-bridges more conveniently, free energy is taken to be a function of $\boldsymbol{C}_e$, as well (ref. Section 2.2). Therefore:

$$\psi = \psi \left(\boldsymbol{C}, \boldsymbol{C}_e, \lambda_a, \beta, \boldsymbol{s}, \mathcal{A}, \mathcal{P}\right) \tag{20}$$

where $\boldsymbol{s} = [R_{\text{off}} \quad D \quad A_1 \quad A_2]^T$. Introducing this function in Eq. (19) gives:

$$\boldsymbol{P} : \dot{\boldsymbol{F}} - \frac{\partial \psi}{\partial \boldsymbol{C}} : \dot{\boldsymbol{C}} - \frac{\partial \psi}{\partial \boldsymbol{C}_e} : \dot{\boldsymbol{C}}_e + \left(P_a - \frac{\partial \psi}{\partial \lambda_a} \right) \dot{\lambda}_a + \left(P_c - \frac{\partial \psi}{\partial \beta} \right) \dot{\beta} - \frac{\partial \psi}{\partial \boldsymbol{s}} \cdot \dot{\boldsymbol{s}} \geq 0 \tag{21}$$

The second and the third terms of this equation can be rewritten as (see Appendix):

$$\frac{\partial \psi}{\partial \boldsymbol{C}} : \dot{\boldsymbol{C}} = 2\boldsymbol{F} \frac{\partial \psi}{\partial \boldsymbol{C}} : \dot{\boldsymbol{F}} \tag{22}$$

$$\frac{\partial \psi}{\partial \boldsymbol{C}_e} : \dot{\boldsymbol{C}}_e = 2\boldsymbol{F}_e \frac{\partial \psi}{\partial \boldsymbol{C}_e} : \dot{\boldsymbol{F}}_e = 2\boldsymbol{F}_e \frac{\partial \psi}{\partial \boldsymbol{C}_e} \boldsymbol{F}_a^{-T} : \dot{\boldsymbol{F}} - 2\boldsymbol{C}_e \frac{\partial \psi}{\partial \boldsymbol{C}_e} \boldsymbol{F}_a^{-T} : \dot{\boldsymbol{F}}_a \tag{23}$$

Back-substitution of Eqs. (22) and (23) into inequality (21) and considering Eq. (12), gives:

$$\left(\boldsymbol{P} - 2\boldsymbol{F} \frac{\partial \psi}{\partial \boldsymbol{C}} - 2\boldsymbol{F} \boldsymbol{F}_a^{-1} \frac{\partial \psi}{\partial \boldsymbol{C}_e} \boldsymbol{F}_a^{-T} \right) : \dot{\boldsymbol{F}} +$$
$$\left(P_a - \frac{\partial \psi}{\partial \lambda_a} + 2\boldsymbol{C}_e \frac{\partial \psi}{\partial \boldsymbol{C}_e} \boldsymbol{F}_a^{-T} : \frac{\partial \boldsymbol{F}_a}{\partial \lambda_a} \right) \dot{\lambda}_a + \left(P_c - \frac{\partial \psi}{\partial \beta} \right) \dot{\beta} - \frac{\partial \psi}{\partial \boldsymbol{s}} \cdot \dot{\boldsymbol{s}} \geq 0 \tag{24}$$

In order to satisfy the above inequality under elastic conditions:

$$\left(\boldsymbol{P} - 2\boldsymbol{F} \frac{\partial \psi}{\partial \boldsymbol{C}} - 2\boldsymbol{F} \boldsymbol{F}_a^{-1} \frac{\partial \psi}{\partial \boldsymbol{C}_e} \boldsymbol{F}_a^{-T} \right) = 0 \tag{25}$$

Multiplying both sides of Eq. (25) by $\boldsymbol{F}^{-1}$ will provide a constitutive relation for the second Piola–Kirchhoff stress tensor of the system:

$$\boldsymbol{S} = 2 \frac{\partial \psi}{\partial \boldsymbol{C}} + 2\boldsymbol{F}_a^{-1} \frac{\partial \psi}{\partial \boldsymbol{C}_e} \boldsymbol{F}_a^{-T} \tag{26}$$

Also, the assumption of a non-dissipative change in the chemical flux (β) in Eq. (24) provides the following expression:

$$P_c = \frac{\partial \psi}{\partial \beta} \tag{27}$$

By taking the time derivative of the constraint equation relating the cross-bridges states (Eq. (3)) and multiplying the result by an arbitrary multiplier ϖ, then adding to Eq. (24), the constitutive relation for the chemical state variables following the same reasoning as in [8], becomes:

$$\left(-\frac{\partial \psi}{\partial \boldsymbol{s}} + \varpi \boldsymbol{1} \right) \cdot \dot{\boldsymbol{s}} \geq 0 \tag{28}$$

where $\boldsymbol{1} = [1 \quad 1 \quad 1 \quad 1]$. To satisfy Eq. (28) for all evolutions of $\dot{\boldsymbol{s}}$, a positive semi-definite square matrix $\boldsymbol{X}$ is assumed that meets the following condition:

$$\dot{\boldsymbol{s}} \cdot \boldsymbol{X} \dot{\boldsymbol{s}} \geq 0 \tag{29}$$

Comparing Eqs. (28) and (29), the evolution law for the chemical state is:

$$-\frac{\partial \psi}{\partial \boldsymbol{s}} + \varpi \boldsymbol{1} = \boldsymbol{X} \dot{\boldsymbol{s}} \tag{30}$$

Finally, by considering the following constitutive relation, Eq. (24) will be satisfied for all system changes:

$$P_a - \frac{\partial \psi}{\partial \lambda_a} + 2\boldsymbol{C}_e \frac{\partial \psi}{\partial \boldsymbol{C}_e} \boldsymbol{F}_a^{-T} : \frac{\partial \boldsymbol{F}_a}{\partial \lambda_a} = \mathcal{C} \dot{\lambda}_a \tag{31}$$

with $\mathcal{C} \geq 0$ an arbitrary function. In this way, the four constitutive relations (Eqs. (26), (27), (30), and (31)) configure a thermodynamically consistent material model satisfying the inequality (24) for all evolutions of the system variables.

2.5. Specialization of the material model

After establishing the constitutive equations of the chemo-mechanical system, a suitable explicit form of the free energy function needs to be introduced. To that end, an additive form of the free energy [8,41] is considered:

$$\psi = \psi_p\left(\boldsymbol{C}, \mathcal{P}\right) + \psi_a\left(\boldsymbol{C}_e, \mathcal{A}, \boldsymbol{s}\right) + \psi_{XB}\left(\boldsymbol{s}\right) + \psi_c\left(\beta\right) \tag{32}$$

where ψ_p is the energy associated with the passive behavior of the tissues, ψ_a with the active, ψ_{XB} the energy in the cross-bridges and ψ_c the effect of the intracellular calcium flow. As a common way for considering the quasi-incompressible response, the passive term of mechanical energy is additively decomposed into a volumetric (ψ_{vol}) and isochoric parts; and the isochoric-passive part is divided into an isotropic matrix (ψ_p^{iso}) and collagen fiber contribution (ψ_p^{aiso}). An appropriate formulation of the passive strain energy function should be proposed according to the tissue being studied. Since there is no multi-axial passive experimental tests available for a proper definition, the function proposed by Tuset et al. [49] for uniaxial tests is selected:

$$\psi_p = \psi_{vol}\left(J\right) + \psi_p^{iso} + \psi_p^{aiso} \tag{33}$$

$$\psi_{vol}\left(J\right) = \frac{1}{2}C_0\left(J^2 - 1 - 2\ln J\right)$$

$$\psi_p^{iso} = C_1\left(\bar{I}_1 - 3\right) + C_2\left(\bar{I}_1 - 3\right)^2$$

$$\psi_p^{aiso} = C_3\left(\bar{I}_4 - 1\right)^2 + C_4\left(\bar{I}_4 - 1\right)^4$$

where $\bar{I}_1$, $\bar{I}_2$, and $\bar{I}_4$ are the modified strain invariants defined as:

$$\bar{I}_1 = tr\left(\bar{\boldsymbol{C}}\right) \tag{34}$$

$$\bar{I}_2 = \frac{1}{2}\left[\left(tr\bar{\boldsymbol{C}}\right)^2 - tr\left(\bar{\boldsymbol{C}}^2\right)\right]$$

$$\bar{I}_4 = \bar{\boldsymbol{C}} : \left(\boldsymbol{p}_0 \otimes \boldsymbol{p}_0\right) = \boldsymbol{p}_0 \cdot \bar{\boldsymbol{C}}\,\boldsymbol{p}_0 = \bar{\lambda}^2$$

The parameters that define the passive material behavior (Eq. (33)) have been determined for all tissues of the abdominal wall from available experimental data of human samples [49].

The second term in Eq. (32) represents the active free energy associated with the cross-bridge formation and is the generalized form of that in [8]:

$$\psi_a = N\left(\bar{\lambda}_a\right)\left(E_1 s_3 + E_2 s_4\right)\frac{1}{2}\left(\bar{J}_4 - 1\right)^2 \tag{35}$$

where E_1 and E_2 are material coefficients, s_3 and s_4 are chemical states associated with A_1, and A_2 respectively, and $\bar{J}_4$ can be interpreted as an squared elastic stretch:

$$\bar{J}_4 = \bar{\boldsymbol{C}}_e : \left(\boldsymbol{a}_0 \otimes \boldsymbol{a}_0\right) = \boldsymbol{a}_0 \cdot \bar{\boldsymbol{C}}_e\boldsymbol{a}_0 = \bar{\lambda}_e^2 \tag{36}$$

$N\left(\bar{\lambda}_a\right)$ models the effect of myosin and actin filaments overlap. To that end, a Gaussian function has been considered [8]:

$$N\left(\bar{\lambda}_a\right) = e^{-\left(\bar{\lambda}_a - \bar{\lambda}_{opt}\right)^2/2\xi^2} \tag{37}$$

where $\bar{\lambda}_{opt}$ is the optimal overlap that leads to the maximum active force generation, and ξ controls the width of the bell curve.

The third term in Eq. (32) is the cross-bridge free energy function that is additively decomposed assuming no coupling between the states. Furthermore constitutive Eq. (30) is provided for the evolution of chemical states. Literature studies [40] proved that the cross-bridge model presented in Section 2.1 (Eq. (4)) is a particular case of Eq. (30). Therefore, chemical states can be determined by Eq. (4) while thermodynamic compatibility of the system is maintained and there is no need to introduce an explicit form of the cross-bridge free energy function (ψ_{XB}).

The last term of Eq. (32) associated with the energy of the intracellular calcium ion flow, can be considered as a simple quadratic function [8,41]:

$$\psi_c = \frac{1}{2}\beta^2 \tag{38}$$

The constitutive equation for total stress can be derived by substitution of Eq. (32) in Eq. (26):

$$S = S_{vol} + \bar{S}_p + \bar{S}_a \tag{39}$$

$$S_{vol} = 2\frac{\partial \psi_{vol}}{\partial C} \tag{40}$$

$$\bar{S}_p = 2\frac{\partial \bar{\psi}_p}{\partial C} = \tilde{S}_p : \mathbb{P}_c \tag{41}$$

$$\tilde{S}_p = 2\frac{\partial \bar{\psi}_p}{\partial \bar{C}}, \qquad \mathbb{P}_c = \frac{\partial \bar{C}}{\partial C} = J^{-2/3}\left(\mathbb{I} - \frac{1}{3}C \otimes C^{-1}\right)$$

$$\bar{S}_a = F_a^{-1}\frac{2\partial \bar{\psi}_a}{\partial C_e}F_a^{-T} = F_a^{-1}\left(\tilde{S}_a : \mathbb{P}_e\right)F_a^{-T} \tag{42}$$

$$\tilde{S}_a = 2\frac{\partial \bar{\psi}_a}{\partial \bar{C}_e}, \qquad \mathbb{P}_e = \frac{\partial \bar{C}_e}{\partial C_e} = J^{-2/3}\left(\mathbb{I} - \frac{1}{3}C_e \otimes C_e^{-1}\right)$$

As a result, additive decomposition of the Cauchy stress tensor can be obtained by the Piola transformation of S [46]:

$$\sigma = J^{-1}FSF^T = \sigma_{vol} + \bar{\sigma}_p + \bar{\sigma}_a \tag{43}$$

The second constitutive equation is Eq. (31) that accounts for the contraction speed. The arbitrary function $\mathcal{C}$ in this equation is proposed as in [8]:

$$\mathcal{C} = \frac{1}{\mu}(f_1 s_3 + f_2 s_4)N(\lambda_a) \tag{44}$$

where μ, f_1, and $f_2 \geq 0$ are constants. In the aforementioned equation, P_a should be also specified. P_a can be interpreted as the internal energy for overcoming the friction between sliding filaments during contraction and P_a provided by converting chemical energy into mechanical work during the power stroke. Following Karami et al. [8], P_a is defined as:

$$P_a = -\nu s_4\left(\frac{s_3}{\max(s_3)}\right)N(\lambda_a) \tag{45}$$

where ν is a constant (sliding velocity) and P_a is scaled by $\frac{s_3}{\max(s_3)}$ proportional to the cross-bridge formation.

The contraction velocity of the active filament along muscle fiber can be calculated by substituting Eqs. (35), (44), and (45) into Eq. (31):

$$\dot{\lambda}_a = \frac{\mu}{(f_1 s_3 + f_2 s_4)}\left[-\nu s_4\left(\frac{s_3}{\max(s_3)}\right)\right.$$
$$\left. - \left(\frac{\lambda_a - \lambda_{opt}}{\xi^2}\right)\frac{1}{2}(E_1 s_3 + E_2 s_4)\left(\bar{J}_4 - 1\right)^2 \right. \tag{46}$$
$$\left. + \frac{2\lambda_e^2}{J^{2/3}\lambda_a}(E_1 s_3 + E_2 s_4)\left(\bar{J}_4 - 1\right)\right]$$

Finally, P_c can be calculated by substitution of ψ_c from Eq. (38) into Eq. (27):

$$P_c = \beta \tag{47}$$

In the end, when the evolution of calcium concentration is determined experimentally ($\beta = \left[Ca^{2+}\right]$ in Eq. (47)), the calcium-dependent rates k^{off} and k^{on} can be obtained. Then, the chemical states can be also calculated from Eq. (4) considering the constraint equation (3) and initial values $[0.999997, 1 \cdot 10^{-5}, 1 \cdot 10^{-5}, 1 \cdot 10^{-5}]$ for $[R_{\text{off}}, D, A_1, A_2]$, with the hypothesis that the muscle activates from a resting condition. Therefore, it is possible to find the contraction velocity (Eq. (46)) assuming that at the beginning of the contraction process $\dot{\lambda}_a = 0$ and subsequently to update muscular fiber stretch (λ_a) and the active contraction tensor (Eq. (10)). On the other hand, the total deformation gradient of the system is known by considering specific boundary conditions and external deformations of the particular model geometry under study. Thereupon, total stress will be available by Eq. (43).

Table 1
Cross-bridge kinetic parameters for abdominal skeletal muscles.

Muscle	k_0^{on} (s^{-1})	k_{Ca}^{on} (s^{-1})	k_0^{off} (s^{-1})	k_{Ca}^{off} (s^{-1})	f (s^{-1})	f' (s^{-1})	h (s^{-1})	h' (s^{-1})	g (s^{-1})
RA	0	35.213	38.300	230.739	108.591	586.043	9.255	17.696	9.726
EO IO-TA	0	31.185	12 800	14.603	21.425	956.195	14.748	4.535	38.060

3. Numerical model of the abdominal wall

3.1. Material parameters

The material model was implemented in the ABAQUS software as a UMAT subroutine. Determining the appropriate material parameters for both the chemical and mechanical part is the next important step. The parameters related to the chemical model (k_{Ca}^{off}, k_0^{off}, k_{Ca}^{on}, k_0^{on}, [Ca$_{50}^{2+}$], p, f, f', h, h' and g) are needed for the definition of Eqs. (1), (2) and (4). Regarding the mechanical part, the required parameters (C_0, C_1, C_2, C_3, C_4, E_1, E_2, $\bar{\lambda}_{opt}$ and ξ) appear in Eqs. (33), (35) and (37). Some of these parameters were determined directly from the literature and others fitted to available experimental data as described in the following sections.

3.1.1. Parameters of the chemical model

The distribution of calcium ions in skeletal muscles and muscles' reaction to the available level of calcium ion concentration depend on the fast or slow behavior of muscles [44,50]. There are limited experimental studies about intracellular calcium ion distribution in human abdominal muscles and especially considering the fact that contraction times in human muscles are different from that of animals, it is difficult to establish reference values. Moreover, abdominal muscles in different animal species also differ in terms of fast or slow-twitch [51–53]. Therefore, in this study, the best attempt was made to extract the required laboratory data from the studies performed on human. According to experimental findings about the distribution of muscle fiber types [54,55] and based on contraction velocity and resting potential [56], human abdominal muscles are generally considered as slow type.

Experimental results of Nikolić et al. [57] showed that the proportion of fast and slow fibers in intercostal muscles is almost the same as in abdominal muscles. To that end, recorded calcium transition in human intercostal muscle [58] was taken as the calcium ion distribution in this study. Then the maximum of Ca^{2+} transition was scaled to $pCa_{max} = 4.994$ based on the available experimental data of calcium ion concentration in human slow skeletal muscles and necessary parameters of $pCa_{50}^{2+} = 6.41869$ and $p = 3.2$ were obtained by curve fitting to the related experimental force-calcium relationship [53][1]

In the proposed model for chemo-mechanical behavior of skeletal muscles, parameters related to the cross-bridge kinematics mainly control the form of contraction in the muscles [44,50,59] while mechanical parameters govern the amplitude of the active force. On the other hand, there is only a few experimental data for the active behavior of abdominal muscles [16,17,19]. Thus, cross-bridge parameters have been determined by fitting the scaled output of the isometric contraction model to the normalized experimental response of EO and RA active force [19]. A nonlinear least-square fitting strategy with initial guesses from [50] and [8] was applied. The parameters for TA and IO have been considered the same as those for the EO (Table 1).

3.1.2. Parameters of the mechanical model

After determination of the cross-bridge parameters, the model was used to fit the experimental active forces determined for RA and EO by Grasa et al. [19]. Since only data for isolated RA and EO was provided in that paper, the active response of TA was determined using the EO results scaled with available data of the maximum isometric force of TA [16]. Active parameters for IO were considered similar to those of EO (Table 2). ξ parameter in Eq. (37) was determined by fitting the experimental force-length diagram to the numerical relationship [17,19] (Table 2).

Passive mechanical parameters were selected from those in [49] obtained using human abdominal tissues (Table 3).

---

[1] $pCa = -\log([Ca^{2+}])$.

Table 2
Material parameters of the mechanical active behavior model for the abdominal skeletal muscles.

Muscle	E_1 (MPa)	E_2 (MPa)	ν (MPa)	f_1 (MPa s)	f_2 (MPa s)	μ (−)	ξ (−)	λ_{opt} (−)
RA	38.96	89.78	27.401	17.98	1.08	2.03	0.1814	1
TA	65.24	36.04	58.83	0.01	31.63	2.64	0.2413	1
EO-IO	119.8	68.4	32.8	1	21.19	1.5	0.1383	1

Table 3
Material parameters of the mechanical passive behavior for the abdominal skeletal muscles [49].

Tissue	C_0 (MPa)	C_1 (MPa)	C_2 (MPa)	C_3 (MPa)	C_4 (MPa)
LA	100	0.05	11	0.1	34
RS	100	0.05	4.7	0.01	0.95
EO	1	0.0021	0.012	0.0029	0.0005
IO	1	0.0021	0.016	0.0053	0.0015
RA	1	0.0021	0.024	0.0092	0.052
TA	1	0.0021	0.019	0.0031	0.0004

Table 4
Preferential directions of tissue fibers referred to cranial-caudal line [19,20,62].

Tissue	TA	IO	EO	RA	APO	RSH	LA
Muscular fiber	90°	±45°	±45°	0°	–	–	–
Collagen fiber	90°	±45°	±45°	0°	±45°	Anterior layer: ±45° Posterior layer: 90°	Anterior layer: ±45° Posterior layer: 90°

3.2. Model geometry

The geometry of abdominal muscles (EO, IO, TA, and RA) and linea alba (LA) were downloaded as OBJ files from [60] website. BodyParts3D [60] is an open-access 3D structure database of body parts that were created from a set of 2 mm interval MRI images of a male volunteer [61]. Model parts have been developed from these 3D volumes for simulation in Abaqus (SIMULIA, Dassault systems) software (Fig. 3). The Rectus sheath (RSH) was modeled on both sides of the RA as a reinforcement layer by means of membrane elements with 450 micrometer thickness [62]. The abdominal cavity was modeled as a volume that overlapped the internal surface of the abdominal wall and is enclosed with the internal surface of the diaphragm on the top and a flat surface modeling the pelvis on the bottom. Intra-abdominal pressure (IAP) was simulated using hydrostatic fluid elements (fluid cavity behavior) inside the abdominal cavity and characterized by a 0.001 g/mm^3 density [63] and a bulk modulus of 8 MPa [36].

Muscle layers were in frictionless contact with each other and tied to connective tissues. The abdominal cavity is also tied to the internal surface of the abdominal wall and fixed at the bottom and at the back to model the supporting effect of the vertebral column. The upper, lower, and lateral sides of the abdominal wall were connected to bony parts such as ribs and pelvis or tight connective tissues such as inguinal ligament, thoracolumbar fascia, and costal cartilage. Thus, all these free edges were considered fixed [64].

Fiber orientations of the different tissues were defined at every integration point in a way that fibers were tangent to the part surface (Figs. 3 and 4) and their preferential direction referred to the cranial-caudal line define the angles showed in Table 4.

Apart from APO, which has a very complex geometry and was meshed using Abaqus C3D10H element type and RSH that was meshed with membrane element type (M3D4H), the other parts of the model were meshed with C3D8H one. After performing a mesh sensitivity study varying the element size, the final model consists of 91 853 elements and 61 743 nodes.

3.3. Reference geometry

The shape that the soft tissues of the abdominal wall adopt in a relaxed state is the result of the equilibrium between the IAP, the external forces and the internal passive stress state of the tissues. To the best of the authorsFL
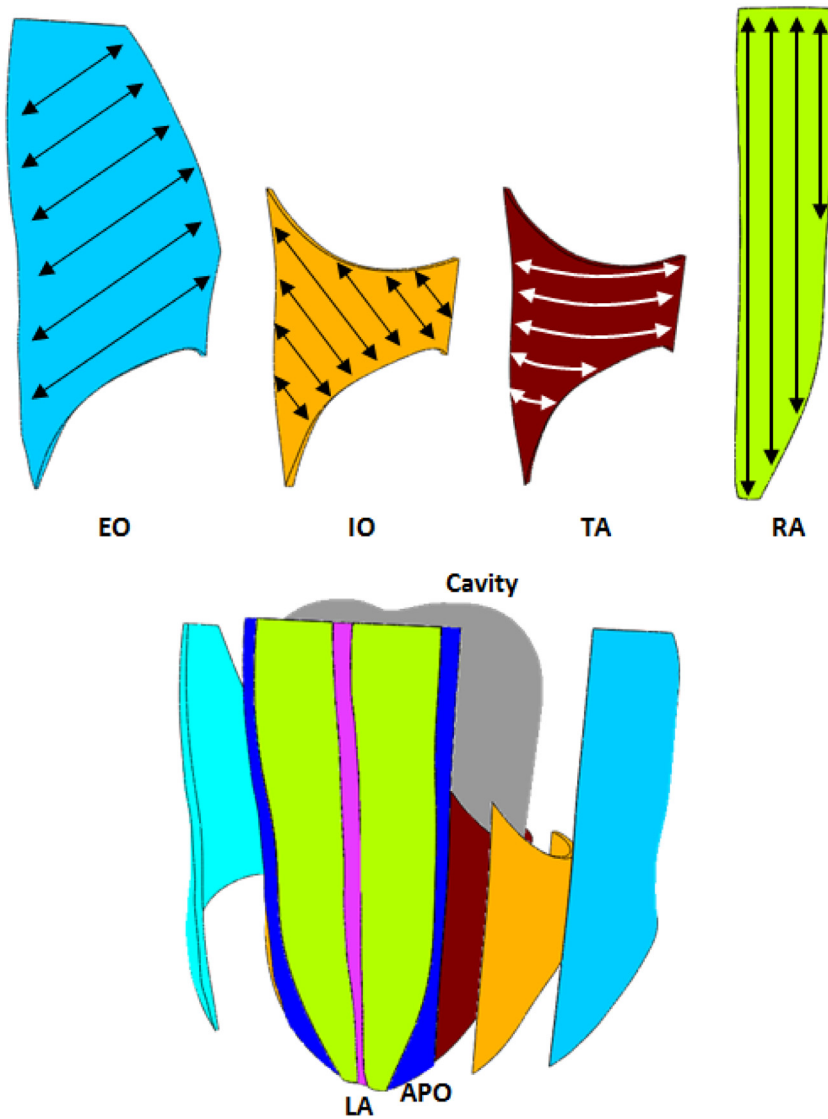
Fig. 3. Parts of the model obtained from [60]: external oblique (EO), internal oblique (IO), transverse abdominis (TA), rectus abdominis (RA), linea alba (LA), aponeurosis (APO) and abdominal cavity. Arrows illustrate the orientation of muscle fibers.

knowledge, there is no experimental data that surveys these stresses in the human abdominal wall since when the geometry of the tissues is segmented from medical image, this state is neglected. Therefore, an accurate stress analysis of the tissues should incorporate the initial state of stress present on the image-based geometry. To determine this distribution, a numerical iterative process [65] was applied to find this configuration. The 3D geometry was obtained in a supine position and an IAP of about 1.8 mmHg [5] was assumed. If the obtained geometry from MRI images is considered as the reference configuration (X_{REF}), the idea was to find an initial stress-free geometry (X_i) in a way that after deforming due to the supine IAP (X_d), it will match the reference configuration ($X_{\text{REF}} = X_d$) [65]. The flowchart of this numerical iterative process for finding the initial stresses is shown in Fig. 5.

To that end, the first iteration is started with the reference configuration ($X_1 = X_{\text{REF}}$) and its corresponding fiber orientations (muscle ($\mathcal{A}_1$) and collagen ($\mathcal{P}_1$) fibers). Supine IAP is applied to the first geometry (X_1) and the first deformed model (X_d^1) is detected. Iteration error is then quantified as the difference between the deformed configuration and the reference one ($E_1 = X_d^1 - X_{\text{REF}}$). For the next iteration, nodal coordinates are updated
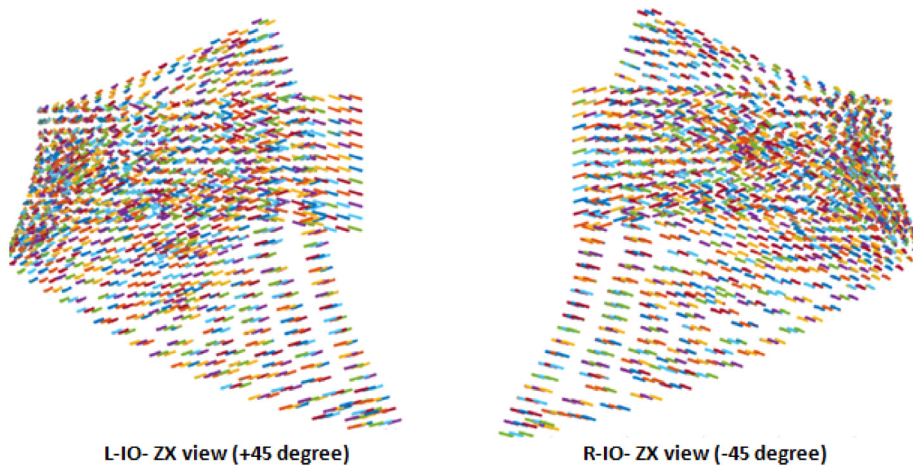
Fig. 4. Orientation of muscle fibers in left (L-IO) and right IO (R-IO). Muscle fibers on the left and right sides of the body look anti-symmetric with respect to the sagittal plane.

considering the previous error ($X_2 = X_1 - E_1$) and local orientation of material anisotropy ($\mathcal{A}_2$ and $\mathcal{P}_2$) are subsequently recalculated. The iterative algorithm (Fig. 5) updates the initial geometry (X_{i+1}) until the infinite norm of the nodal error ($e_i = \parallel X_d^i - X_{\text{REF}} \parallel_\infty$) is less than or equal to the tolerance ($e_i \leq Ite_{\text{TOL}}$) or the number of repetitions exceeds the desired number ($i > Ite_{\max}$).

In an ideal supine position, there is no active contraction in abdominal muscles [66]. Hence, the active behavior of the muscles was neglected in the simulations for finding the stress-free configuration.

4. Results

4.1. Reference tissue geometry

Fig. 6 illustrates the iterative process proposed for finding the reference geometry which incorporates tissue stresses to achieve the equilibrium with the IAP as provided by the MRI. At first iteration (Fig. 6(a)), there is a maximum value of 9 millimeter distance between the MRI image in the supine position (reference geometry) and the model geometry under supine IAP. Applying the iterative algorithm (5), this error was decreased by an 88% (Fig. 6(b)). Active muscle behavior is ignored in the supine position [66]. The effect of this assumption can also be seen in Fig. 6. The deviation of lateral muscles under supine IAP in the first iteration (Fig. 6(a)) is much less than that of the upper and lower regions (epigastric and hypogastric) of the abdomen that are covered by the RSH and LA. The stresses that compensate for this undesired displacement hence is negligible in lateral muscles. In contrast with the lateral muscles, the amount of stress in LA, RSH, and the RA muscle that is affected by the deformation of RSH, is noteworthy. Stress contours of these three parts (RA, RSH, LA) are shown in Fig. 7.

4.2. Cough in the supine position

To evaluate the performance of the model, a coughing state in the supine position is simulated. Chemical states of each muscle are determined by solving its ODEs (Eqs. (3) and (4)) for an experimental Ca^{2+} transient [58]. In the simulation, muscles are activated based on their specific s_3 and s_4 states that are scaled according to the experimentally recorded percentage of normalized EMG for that muscle [67]. Therefore every muscle is activated exclusively based on its chemo-mechanical response and subject-specific control. To analyze the effect of the stresses in the tissues, two scenarios have been considered with and without initial stresses. The geometries considered at the beginning of the simulations for these two scenarios are not the same. While the reference geometry is directly taken for the model without initial stresses, the model considering initial stresses establishes a previous fictitious geometry that requires the action of the IAP to attain the reference geometry. The induced pressure inside the abdominal cavity due to the activity of the muscles is shown in Fig. 8.
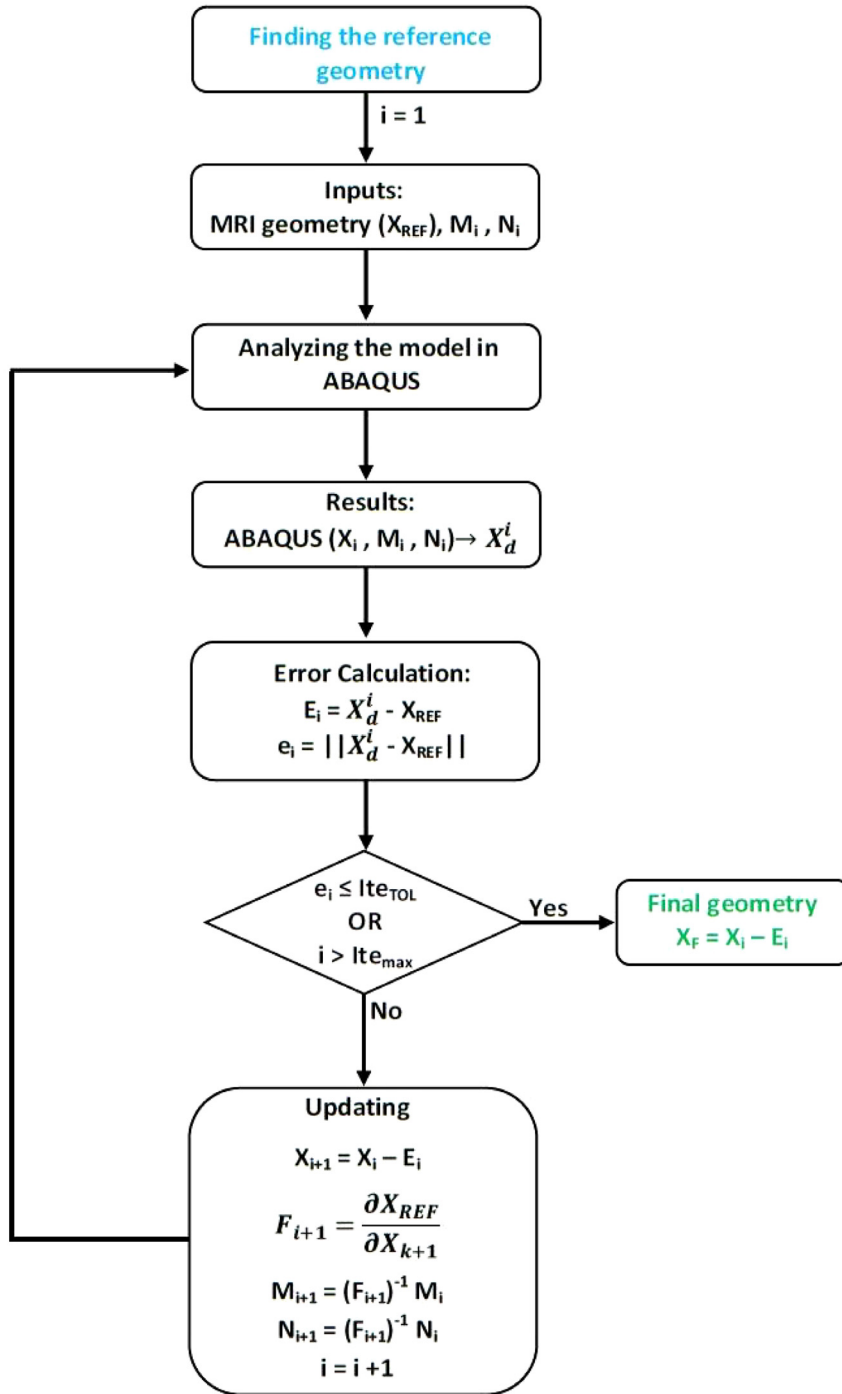
Fig. 5. Flowchart of the iterative process for finding the reference geometry in the model.

In Fig. 8, when ignoring initial stresses (solid line with dots), Ca^{2+} signal is applied to the reference configuration from the beginning of the simulation. IAP starts to increase due to the muscle contraction and reaches its maximum after 0.2 s. In the case of considering the initial stresses (dotted plot), on the other hand, the simulations has been divided in two steps. In the first step (from $t = 0$ s to $t = 0.5$ s), the initial stress-free geometry deforms due to the

(a) First Iteration   (b) Final Iteration
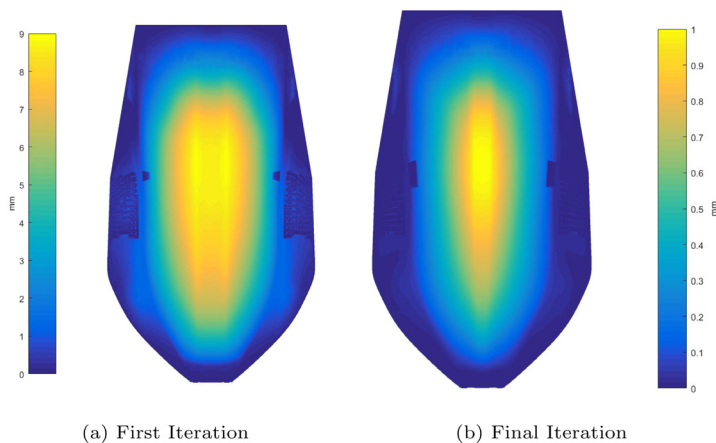
Fig. 6. Distance contour between MRI in supine position (reference geometry) and simulated geometry of abdominal wall under supine IAP, in the first and the last iteration of the iterative process.
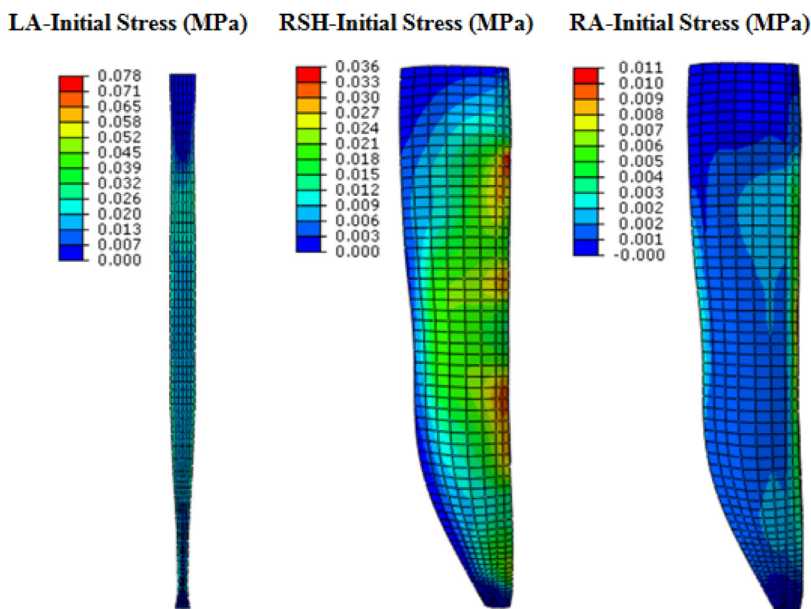

Fig. 7. The initial stresses generated in the tissues of the linea alba (LA), rectus sheath (RSH), and rectus muscle (RA) under supine IAP.

supine IAP (1.8 mmHg [5]) and transforms to the reference configuration. At this point ($t = 0.5$ s), the coughing step starts by applying the Ca^{2+} signal to the model. IAP, therefore, increases due to the muscle contraction and reaches its maximum level at $t = 0.65$ s (Fig. 8).

Fig. 9 shows the displacement contour of these two simulations. The maximum amount of displacement is approximately the same in both simulations and occurs at the flank when abdominal wall moves inward due to the fiber orientation effects; however, considering the stresses they change the pattern of movement in the upper and lower abdomen.

Figs. 10 and 11 display stress contours for connective tissues and muscles of the abdominal wall in both simulations, respectively. Maximum principal stress of TA, IO, and EO when ignoring the initial stresses are respectively 0.7095, 0.396, and 0.0759 MPa. These results are slightly lower than their corresponding ones when considering the initial stresses. TA, IO, and EO muscles experienced maximum principal stresses of 0.6588, 0.3507, and 0.0724 MPa, respectively when initial stress is considered. However, the pattern and magnitude of generated
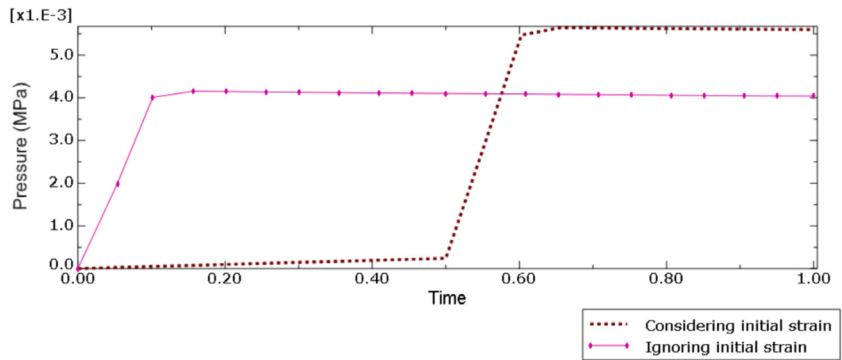
Fig. 8. Simulated pressure in the abdominal cavity during cough in supine position: considering (dotted line) and ignoring (solid line) initial strain.
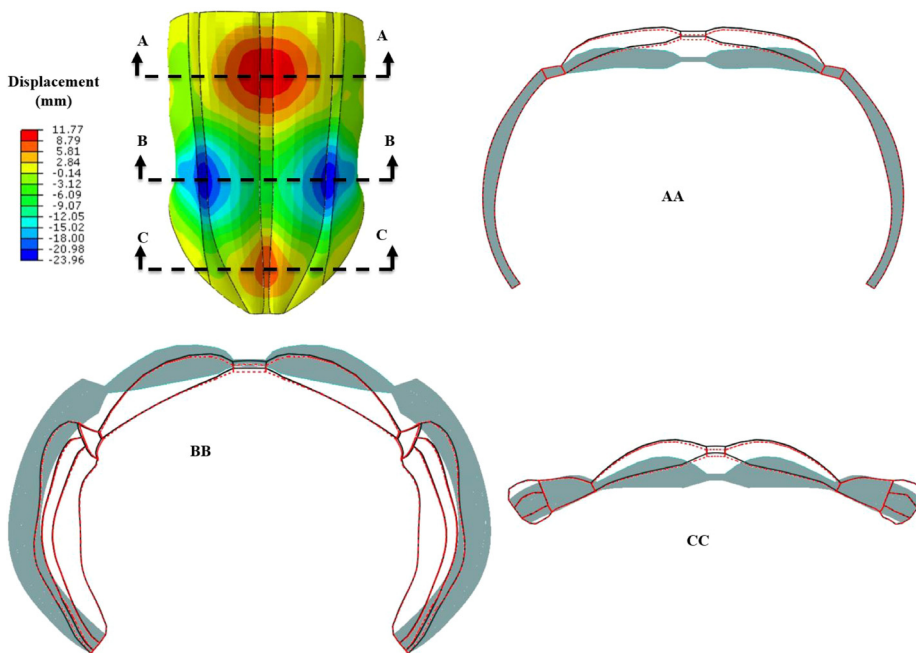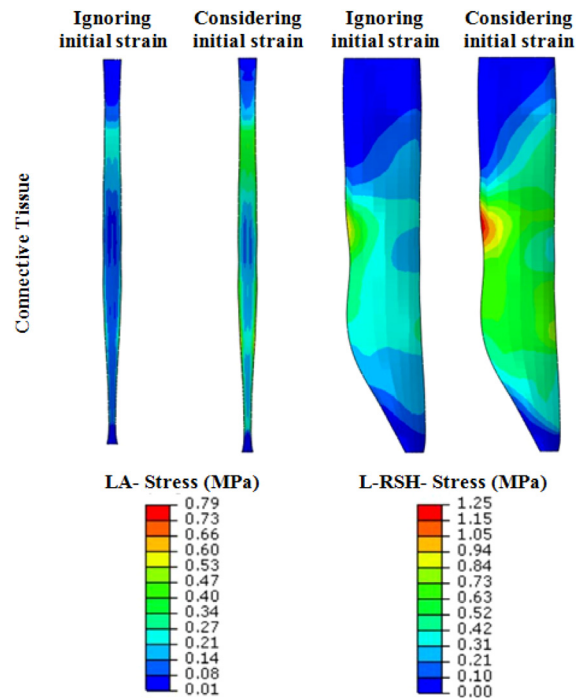

Fig. 9. Displacement of the abdominal wall during cough in supine position; comparison between supine state (gray filled), considering the initial stresses (black solid line) and ignoring them (red dashed line) in three cross sections.

stresses in RA muscle, RSH, and LA tissues are more seriously affected by the initial stresses. LA undergoes a larger stress of 0.407 MPa by applying the initial stresses, in comparison to 0.2362 MPa when they are not considered. A similar effect has occurred for the RSH (0.9154 MPa versus 0.612 MPa with and without initial stresses, respectively) and, to some extent, for the RA muscle enclosed by its sheath (0.0382 MPa versus 0.0362 MPa with and without initial stresses, respectively).

5. Discussion

The multi-scale chemo-mechanical model proposed in this work provides the possibility of stimulating abdominal wall muscles by a calcium signal that can be related with the electrical activity of the tissues. A previous 2D multi-scale material model [8] was successfully extended into a 3D model and implemented in the commercial FE software Abaqus. As shown, the trigger of the chemical activity was related to real EMG signals that can be applied

Fig. 10. Maximum principal stress contour in abdominal wall connective tissues during cough in supine position; comparison between considering the initial stresses and ignoring them. L: Left, RSH: Rectal sheath, LA: Linea alba.

selectively thorough different muscles. This allowed to find the overall response of a particular muscle group, in this case the contraction of the abdominal wall but it could be extended to obtain the movement of any joint controlled by its agonist and antagonist muscles. Furthermore, the model accounted for the initial or internal stresses in the tissues that make it possible to achieve more realistic results. To the best of the authorsFL knowledge, no model has been previously proposed that can predict the internal pressure of the abdominal cavity in this way.

According to Fig. 8, incorporating the effect of the initial stresses in the tissues of the abdominal wall conducted to higher intra-abdominal pressure with the same amount of muscle activity. Initial stresses were only a consequence of the equilibrium of the passive behavior of tissues since the active behavior of muscles was disregarded in the determination of the reference configuration. In comparison to the muscles, connective tissues have much larger passive stiffness [49]. Thus, muscles played a minor role in establishing the reference configuration defined in this work.

The stress distribution in the EO, IO, and TA muscles, that have trivial effect on the reference configuration, did not shown a significant difference with or without considering the initial stresses (Fig. 11). However, the deformation of the rectus sheath due to initial strain was to some extent transferred to the rectus muscle. Therefore, rectus behavior was more affected by initial stresses in comparison with the other muscles and its stress distribution was slightly different in the two simulated conditions (Fig. 11).

The main difference in the displacement field between the two simulations (Fig. 9) occurred in the middle region of the abdomen. While disregarding initial stresses, connective tissues of the linea alba and rectus sheath were deformed slightly. Thus, they withstand less stress levels (Fig. 10) and they played a discreet role in withstanding internal pressure. By applying initial stresses, deformation of connective tissues (Fig. 9), their final stress distribution (Fig. 10) and consequently, their participation in enduring internal pressure of the abdomen increased.

For simulating the coughing effect, the levels of calcium ion activation for the different muscles of the abdominal wall were adjusted according to EMG data provided by Neumann and Gill [67] in the supine position (Table 5). In this way, the muscles received different levels of activation according to their physiological electrical activity. The predicted IAP was 42 mmHg when considering initial stresses and matches with the experimentally reported pressure in [67] (46 mmHg). This pressure was significantly different from the mean IAP reported in [5] (81.4
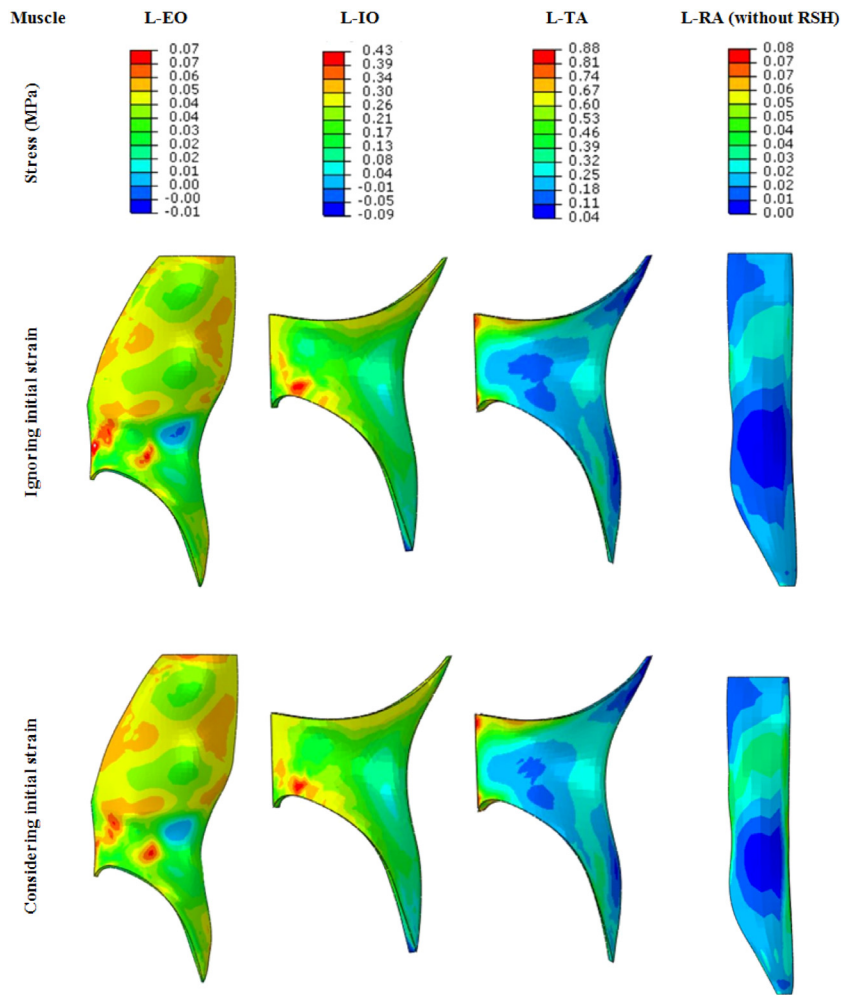
Fig. 11. Maximum principal stress contours in the abdominal wall muscles during cough in supine position; without considering the initial stresses (top) and considering them (bottom). L: Left, EO: external oblique muscle, IO: internal oblique muscle, TA: transverse abdominis muscle, RA: rectus abdominis muscle, RSH: rectus sheath.

Table 5
Normalized (%) EMG of abdominal wall muscles during cough in the supine position [67].

Muscle	EO	IO	TA	RA
Normalized (%) EMG	56	136	179	26

mmHg) for coughing in sitting posture. One of the reasons for this difference can be due to dissimilar test posture, cough in supine (presented simulation and [67]), and sitting position [5]. Considering the fact that the measured IAP during coughing in standing position is higher than sitting condition [5], it is expected that IAP to be the lowest during coughing in supine posture in line with the simulated result.

Experimental studies show that the IAP decreases from the upright position (midline angle with horizon = 90°) to the supine position (midline angle with horizon = 0°) significantly [66,68]. Elimination of the organs' gravitational forces in the thoracic cavity from the top of the diaphragm and abdominal cavity can be an explanation for this observation [66,69]. This subject is probably a reason for less IAP during cough in a supine position compare to a sitting posture and similarly less IAP during cough in a sitting state in comparison with a standing posture. On the other hand, the activation of pelvic floor muscles (PFM) at the bottom of the abdominal cavity has a significant effect

on the IAP. PFM activated about 64% during cough in supine state [67]. Perhaps, the anatomical position of PFM during cough in standing and sitting postures lets more contraction as compared to a supine state and consequently, higher IAP is generated. As considered in the model, the pelvic floor induces a fixed boundary condition that could be assumed as a fully activation of PFM. This boundary condition simplifies its effects on the IAP and for a more precise study of the abdominal cavity the contraction of these muscles should be incorporated. The role of internal organs also requires further analysis as its behavior could affect the evolution of IAP. As hydrostatic fluid elements were used to represent the cavity volume with a relative high bulk modulus, the compliance of these organs will determine the transient behavior of the pressure over time.

Another important reason for the discussed difference is the relevance of subjects' body mass index (BMI) in the abdominal cavity pressure. Experimental studies [5,66,70] showed that there is a direct relationship between a person's body mass index (BMI) and an increase in his abdominal pressure. In the research of Neumann and Gill [67], due to the limitations of the test conditions, the subjects were selected from lean individuals (BMI < 20). However, Cobb et al. [5] recruited subjects with various BMI to investigate the relationship between intra-abdominal pressure and BMI. The average BMI of the subjects in [5] was equal to 24.6 kg/m^2 (range 18.4–31.9 kg/m^2). This BMI is close to the category of overweight people. On the other hand, the high standard deviation reported for sitting cough condition in [5] could also indicate variation in recorded intra-abdominal pressures due to subjects' BMI. The positive correlation between higher BMI and increased IAP [5] indicates the effect of the fat layer in the abdominal wall on IAP. Fat tissue does not have an active role on the IAP but its passive properties could influence the IAP. Since the EMG signals correspond to lean subjects [67], the fat tissue has not been considered. For a subject-specific model, it is recommended to take the role of fat tissue according to the MRI scans into account. Furthermore, this study assumed that healthy skin has a highly compliant behavior and would not significantly contribute to IAP changes during normal tasks such as coughing. However, in special cases such as pregnancy or burn-induced compartment syndrome (due to severe burn) when skin reaches its critical range of resilience, it would be necessary to model the role of skin for studying the IAP. Another important effect that has not been considered in the model is related to another important tissue present in the abdominal wall. The fascia layer that wraps the muscle tissue, due to its slippery nature, was considered to have a frictionless influence between layers of tissue. Therefore, it was assumed that the force developed in abdominal muscles was transferred without any dissipation and there is no effect to the IAP evolution.

There are few studies in the literature that simulated the human abdominal cavity with a real geometry and considered both active and passive behavior of muscles [35,36]. The results of the present model showed that by considering active behavior of the muscles into account, abdominal wall displacement in posterior–anterior direction decreased significantly in comparison with the models that only simulate passive behavior of the muscles [33–35]. The main reason for this finding was the increase in stiffness and strength of the abdominal wall due to the active behavior of the muscles. Thus, the abdominal wall moves less for a certain pressure when the muscles are activated. Consequently, it will be necessary to consider the active behavior of the muscles for performing various medical studies on the abdominal wall and investigating its relevant abnormalities such as hernia, its causes, treatment, and prevention.

Because of the RA muscle activation with vertical fibers (along the cranio-caudal direction), the anterior region of the abdomen contracted inwards in the model. Moreover, the activity of the lateral muscles in the abdominal wall (TA, EO, IO) caused their oblique fibers to shorten which leads to the contraction of the abdominal wall inwardly, especially at the flank (Fig. 9). These features cannot be simulated if the active behavior of muscles is excluded and the abdominal wall will shift only outward by an increase in internal pressure.

In addition to the several advantages of numerical simulations, there is always a big challenge in the provision of appropriate experimental data for determining the coefficients of the model. Inaccuracy in gathering the empirical data, inherent variation among individuals, and mathematical approximations cause uncertainties in the model parameters [71] and there is no exception to the presented model. Therefore, it is important to consider further details into account for attaining more realistic results and patient-specific models.

6. Conclusions

The presented 3D multi-scale chemo-mechanical material model is able to take advantage of the real EMG to predict the active response of skeletal muscles. The material model is successfully implemented in a 3D realistic geometry of the abdominal cavity. It has been reported that in an ideal supine position, abdominal muscles are

relaxed and do not have any active behavior. As a result, the initial stresses are estimated without considering active muscle contraction. Incorporating the effect of the initial strains in the tissues of the abdominal wall allowed for the attainment of more realistic IAP values according to experimental outcomes. Nonetheless, stress and displacement results show less sensitivity to the initial stresses effect. The results depict the importance of muscles' active behavior in the tolerance of IAP and in control of the abdominal wall displacement under the IAP.

Declaration of competing interest

Data availability

Data will be made available on request.

Acknowledgments

Appendix

Following the index notation prepared in [72], the second term of Eq. (21) can be rearranged as:

$$
\begin{aligned}
\frac{\partial \psi}{\partial \mathbf{C}} : \dot{\mathbf{C}} &= \left(\frac{\partial \psi}{\partial C}\right)_{IJ} \frac{\partial (F^T F)_{IJ}}{\partial t} = \left(\frac{\partial \psi}{\partial C}\right)_{IJ} \left(\dot{F}^T F + F^T \dot{F}\right)_{IJ} \\
&= \left(\frac{\partial \psi}{\partial C}\right)_{IJ} \left(\dot{F}^T_{Ii} F_{iJ} + F^T_{Ii} \dot{F}_{iJ}\right) = F_{iJ} \left(\frac{\partial \psi}{\partial C}\right)_{IJ} \dot{F}_{iI} + F_{iI} \left(\frac{\partial \psi}{\partial C}\right)_{IJ} \dot{F}_{iJ} \\
&= 2\mathbf{F}\left(\frac{\partial \psi}{\partial \mathbf{C}}\right)\dot{\mathbf{F}}
\end{aligned}
\tag{A.1}
$$

and to make $\dot{\mathbf{F}}$ and $\dot{\mathbf{F}}$ subjects of the third sentence in Eq. (21), rearrangement can continue as:

$$
\begin{aligned}
\mathbf{F_e} \frac{\partial \psi}{\partial \mathbf{C_e} : \dot{\mathbf{F}_e}} &= (F_e)_{iI} \left(\frac{\partial \psi}{\partial C_e}\right)_{IJ} \left(\dot{F}_e\right)_{iJ} = \\
&\underbrace{\left(F F_a^{-1}\right)_{iI} \left(\frac{\partial \psi}{\partial C_e}\right)_{IJ} \left(\dot{F} F_a^{-1}\right)_{iJ}}_{A} + \underbrace{\left(F F_a^{-1}\right)_{iI} \left(\frac{\partial \psi}{\partial C_e}\right)_{IJ} \left(F \dot{F}_a^{-1}\right)_{iJ}}_{B}
\end{aligned}
\tag{A.2}
$$

$$
\begin{aligned}
A &\equiv F_{iM} \left(F_a^{-1}\right)_{MI} \left(\frac{\partial \psi}{\partial C_e}\right)_{IJ} \dot{F}_{iN} \left(F_a^{-1}\right)_{NJ} = F_{iM} \left(F_a^{-1}\right)_{MI} \left(\frac{\partial \psi}{\partial C_e}\right)_{IJ} \left(F_a^{-T}\right)_{JN} \dot{F}_{iN} = \\
&\left(\mathbf{F F_a^{-1}}\right) \frac{\partial \psi}{\partial \mathbf{C_e}} \mathbf{F_a^{-T}} : \dot{\mathbf{F}}
\end{aligned}
$$

Part B can be simplified by using $\dot{\mathbf{F}_a^{-1}} = -\mathbf{F}_a^{-1}\dot{\mathbf{F}}_a\mathbf{F}_a^{-1}$ [46] as:

$$
\begin{aligned}
B &\equiv \left(FF_a^{-1}\right)_{iI}\left(\frac{\partial\psi}{\partial C_e}\right)_{IJ}\left(-FF_a^{-1}\dot{F}_aF_a^{-1}\right)_{iJ} \\
&= -\left(F_{iM}\left(F_a^{-1}\right)_{MI}\right)\left(\frac{\partial\psi}{\partial C_e}\right)_{IJ}\left(F_{iN}\left(F_a^{-1}\right)_{NO}\left(\dot{F}_a\right)_{OR}\left(F_a^{-1}\right)_{RJ}\right) \\
&= -\left(F_a^{-T}\right)_{ON}F_{Ni}^T F_{iM}\left(F_a^{-1}\right)_{MI}\left(\frac{\partial\psi}{\partial C_e}\right)_{IJ}\left(F_a^{-T}\right)_{JR}\left(\dot{F}_a\right)_{OR} \\
&= \left(\mathbf{FF_a^{-1}}\right)^{\mathbf{T}}\left(\mathbf{FF_a^{-1}}\right)\left(\frac{\partial\psi}{\partial\mathbf{C_e}}\right)\mathbf{F_a^{-T}} : \dot{\mathbf{F}}_\mathbf{a} = \mathbf{C_e}\left(\frac{\partial\psi}{\partial\mathbf{C_e}}\right)\mathbf{F_a^{-T}} : \dot{\mathbf{F}}_\mathbf{a}
\end{aligned}
$$

References

[1] F.H. Netter, Atlas of Human Anatomy, in: (Netter Basic Science), 2006.

[2] S. Kalaba, E. Gerhard, J.S. Winder, E.M. Pauli, R.S. Haluck, J. Yang, Design strategies and applications of biomaterials and devices for hernia repair, Bioact. Mater. 1 (2016) 2–17.

[3] W. He, X. Liu, S. Wu, J. Liao, G. Cao, Y. Fan, X. Li, A numerical method for guiding the design of surgical meshes with suitable mechanical properties for specific abdominal hernias, Comput. Biol. Med. 116 (2020) 103531.

[4] C. García-García, M. Carrascal-Morillo, J.C. Gómez, C.B. Guerrero, J.G. Prada, An approach to evaluating and benchmarking the mechanical behavior of a surgical mesh prototype designed for the repair of abdominal wall defects, J. Mech. Behav. Biomed. Mater. 125 (2022) 104909.

[5] W.S. Cobb, J.M. Burns, K.W. Kercher, B.D. Matthews, H.J. Norton, B.T. Heniford, Normal intraabdominal pressure in healthy adults, J. Surg. Res. 129 (2005) 231–235.

[6] C.R. Deeken, S.P. Lake, Mechanical properties of the abdominal wall and biomaterials utilized for hernia repair, J. Mech. Behav. Biomed. Mater. 74 (2017) 411–427.

[7] L. Tuset, M. López-Cano, G. Fortuny, J.M. López, J. Herrero, D. Puigjaner, Virtual simulation of the biomechanics of the abdominal wall with different stoma locations, Sci. Rep. 12 (2022) 1–9.

[8] M. Karami, B. Calvo, H. Zohoor, K. Firoozbakhsh, J. Grasa, Assessing the role of Ca^2+ in skeletal muscle fatigue using a multi-scale continuum model, J. Theoret. Biol. 461 (2019) 76–83.

[9] T. Förstemann, J. Trzewik, J. Holste, B. Batke, M. Konerding, T. Wolloscheck, C. Hartung, Forces and deformations of the abdominal wall—a mechanical and geometrical approach to the linea alba, J. Biomech. 44 (2011) 600–606.

[10] P. Martins, E. Peña, R.N. Jorge, A. Santos, L. Santos, T. Mascarenhas, B. Calvo, Mechanical characterization and constitutive modelling of the damage process in rectus sheath, J. Mech. Behav. Biomed. Mater. 8 (2012) 111–122.

[11] H.B. Abdelounis, S. Nicolle, M. Ottenio, P. Beillas, D. Mitton, Effect of two loading rates on the elasticity of the human anterior rectus sheath, J. Mech. Behav. Biomed. Mater. 20 (2013) 1–5.

[12] G.M. Cooney, S.P. Lake, D.M. Thompson, R.M. Castile, D.C. Winter, C.K. Simms, Uniaxial and biaxial tensile stress–stretch response of human linea alba, J. Mech. Behav. Biomed. Mater. 63 (2016) 134–140.

[13] M.H.S. Cardoso, et al., Experimental study of the human anterolateral abdominal wall: Biomechanical properties of fascia and muscles, 2012.

[14] C. Hollinsky, S. Sandberg, Measurement of the tensile strength of the ventral abdominal wall in comparison with scar tissue, Clin. Biomech. 22 (2007) 88–92.

[15] A. Levillain, M. Orhant, F. Turquier, T. Hoc, Contribution of collagen and elastin fibers to the mechanical behavior of an abdominal connective tissue, J. Mech. Behav. Biomed. Mater. 61 (2016) 308–317.

[16] G.A. Farkas, D.F. Rochester, Characteristics and functional significance of canine abdominal muscles, J. Appl. Physiol. 65 (1988) 2427–2433.

[17] G.A. Farkas, Mechanical characteristics and functional length of canine expiratory muscles, Respir. Physiol. 90 (1992) 87–98.

[18] J.S. Arnold, A.J. Thomas, S.G. Kelsen, Contractile properties of expiratory abdominal muscles: effect of elastase-induced emphysema, J. Appl. Physiol. 62 (1987) 2314–2319.

[19] J. Grasa, M. Sierra, N. Lauzeral, M. Muñoz, F. Miana-Mena, B. Calvo, Active behavior of abdominal wall muscles: Experimental results and numerical model formulation, J. Mech. Behav. Biomed. Mater. 61 (2016) 444–454.

[20] B. Hernández, E. Peña, G. Pascual, M. Rodriguez, B. Calvo, M. Doblaré, J. Bellón, Mechanical and histological characterization of the abdominal muscle. a previous step to modelling hernia surgery, J. Mech. Behav. Biomed. Mater. 4 (2011) 392–404.

[21] K. Junge, U. Klinge, A. Prescher, P. Giboni, M. Niewiera, V. Schumpelick, Elasticity of the anterior abdominal wall and impact for reparation of incisional hernias using mesh implants, Hernia 5 (2001) 113–118.

[22] M.A. Konerding, M. Bohn, T. Wolloscheck, B. Batke, J.L. Holste, S. Wohlert, J. Trzewik, T. Förstemann, C. Hartung, Maximum forces acting on the abdominal wall: experimental validation of a theoretical modeling in a human cadaver study, Med. Eng. Phys. 33 (2011) 789–792.

[23] F. Podwojewski, M. Ottenio, P. Beillas, G. Guerin, F. Turquier, D. Mitton, Mechanical response of human abdominal walls ex vivo: effect of an incisional hernia and a mesh repair, J. Mech. Behav. Biomed. Mater. 38 (2014) 126–133.

[24] D. Tran, D. Mitton, D. Voirin, F. Turquier, P. Beillas, Contribution of the skin, rectus abdominis and their sheaths to the structural response of the abdominal wall ex vivo, J. Biomech. 47 (2014) 3056–3063.

[25] U. Klinge, M. Müller, C. Brücker, V. Schumpelick, Application of three-dimensional stereography to assess abdominal wall mobility, Hernia 2 (1998) 11–14.

[26] M. Müller, U. Klinge, J. Conze, V. Schumpelick, Abdominal wall compliance after marlex®mesh implantation for incisional hernia repair, Hernia 2 (1998) 113–117.

[27] G. Welty, U. Klinge, B. Klosterhalfen, R. Kasperk, V. Schumpelick, Functional impairment and complaints following incisional hernia repair with different polypropylene meshes, Hernia 5 (2001) 142–147.

[28] D. Tran, F. Podwojewski, P. Beillas, M. Ottenio, D. Voirin, F. Turquier, D. Mitton, Abdominal wall muscle elasticity and abdomen local stiffness on healthy volunteers during various physiological activities, J. Mech. Behav. Biomed. Mater. 60 (2016) 451–459.

[29] S. Todros, N. de Cesare, S. Pianigiani, G. Concheri, G. Savio, A.N. Natali, P.G. Pavan, 3D surface imaging of abdominal wall muscular contraction, Comput. Methods Programs Biomed. 175 (2019) 103–109.

[30] C. Song, A. Alijani, T. Frank, G. Hanna, A. Cuschieri, Elasticity of the living abdominal wall in laparoscopic surgery, J. Biomech. 39 (2006a) 587–591.

[31] C. Song, A. Alijani, T. Frank, G. Hanna, A. Cuschieri, Mechanical properties of the human abdominal wall measured in vivo during insufflation for laparoscopic surgery, Surg. Endosc. Other Interv. Tech. 20 (2006b) 987–990.

[32] R. Simón-Allué, J. Montiel, J. Bellón, B. Calvo, Developing a new methodology to characterize in vivo the passive mechanical behavior of abdominal wall on an animal model, J. Mech. Behav. Biomed. Mater. 51 (2015) 40–49.

[33] B. Hernández-Gascón, A. Mena, E. Peña, G. Pascual, J. Bellón, B. Calvo, Understanding the passive mechanical behavior of the human abdominal wall, Ann. Biomed. Eng. 41 (2013b) 433–444.

[34] P. Pachera, P. Pavan, S. Todros, C. Cavinato, C. Fontanella, A. Natali, A numerical investigation of the healthy abdominal wall structures, J. Biomech. 49 (2016) 1818–1823.

[35] P.G. Pavan, S. Todros, P. Pachera, S. Pianigiani, A.N. Natali, The effects of the muscular contraction on the abdominal biomechanics: a numerical investigation, Comput. Methods Biomech. Biomed. Eng. 22 (2019) 139–148.

[36] S. Todros, N. de Cesare, G. Concheri, A.N. Natali, P.G. Pavan, Numerical modelling of abdominal wall mechanics: the role of muscular contraction and intra-abdominal pressure, J. Mech. Behav. Biomed. Mater. 103 (2020) 103578.

[37] B. Hernández-Gascón, E. Peña, J. Grasa, G. Pascual, J.M. Bellón, B. Calvo, Mechanical response of the herniated human abdomen to the placement of different prostheses, J. Biomech. Eng. 135 (2013c).

[38] R. Simón-Allué, B. Hernández-Gascón, L. Lèoty, J. Bellón, E. Peña, B. Calvo, Prostheses size dependency of the mechanical response of the herniated human abdomen, Hernia 20 (2016) 839–848.

[39] E. Peña, B. Hernández-Gascón, B. Calvo, Human abdomen: Mechanical modeling and clinical applications, in: Biomechanics of Living Organs, Elsevier, 2017, pp. 267–285.

[40] J. Stålhand, A. Klarbring, G.A. Holzapfel, Smooth muscle contraction: mechanochemical formulation for homogeneous finite strains, Prog. Biophys. Mol. Biol. 96 (2008) 465–481.

[41] J. Stålhand, A. Klarbring, G.A. Holzapfel, A mechanochemical 3d continuum model for smooth muscle contraction under finite strains, J. Theoret. Biol. 268 (2011) 120–130.

[42] B. Hernández-Gascón, J. Grasa, B. Calvo, J. Rodríguez, A 3D electro-mechanical continuum model for simulating skeletal muscle contraction, J. Theoret. Biol. 335 (2013a) 108–118.

[43] M.W. Berchtold, H. Brinkmeier, M. Muntener, Calcium ion in skeletal muscle: its crucial role for muscle function, plasticity, and disease, Physiol. Rev. 80 (2000) 1215–1265.

[44] L.C. Rome, Design and function of superfast muscles: new insights into the physiology of skeletal muscle, Annu. Rev. Physiol. 68 (2006) 193–221.

[45] K.B. Campbell, M.V. Razumova, R.D. Kirkpatrick, B.K. Slinker, Nonlinear myofilament regulatory processes affect frequency-dependent muscle fiber stiffness, Biophys. J. 81 (2001b) 2278–2296.

[46] G.A. Holtzapfel, Nonlinear solid mechanics: A continuum approach for engineering, 2000.

[47] E.M. Arruda, K. Mundy, S. Calve, K. Baar, Denervation does not change the ratio of collagen I and collagen III mRNA in the extracellular matrix of muscle, Am. J. Physiol.-Regulatory, Integr. Comp. Physiol. 292 (2001) R983–R987.

[48] P. Germain, The method of virtual power in continuum mechanics. part 2: Microstructure, SIAM J. Appl. Math. 25 (1973) 556–575.

[49] L. Tuset, G. Fortuny, J. Herrero, D. Puigjaner, J.M. Lopez, Implementation of a new constitutive model for abdominal muscles, Comput. Methods Programs Biomed. 179 (2019) 104988.

[50] K.B. Campbell, M.V. Razumova, R.D. Kirkpatrick, B.K. Slinker, Myofilament kinetics in isometric twitch dynamics, Ann. Biomed. Eng. 29 (2001a) 384–405.

[51] D. Aidley, Transient changes in isotonic shortening velocity of frog rectus abdominis muscles in potassium contracture, Proc. R. Soc. Lond. Ser. B. Biol. Sci. 163 (1965) 215–223.

[52] C. Rodrigues, A. Rodrigues Jr., G. Bohm, Effects of aging on muscle fibers and collagen content of the diaphragm: a comparison with the rectus abdominis muscle, Gerontology 42 (1996) 218–228.

[53] A.J. Russell, J.J. Hartman, A.C. Hinken, A.R. Muci, R. Kawas, L. Driscoll, G. Godinez, K.H. Lee, D. Marquez, W.F. Browne, et al., Activation of fast skeletal muscle troponin as a potential therapeutic approach for treating neuromuscular diseases, Nat. Med. 18 (2012) 452–455.

[54] A.S. Colling-Saltin, Enzyme histochemistry on skeletal muscle of the human foetus, J. Neurol. Sci. 39 (1978) 169–185.

[55] T. Häggmark, A. Thorstensson, Fibre types in human abdominal muscles, Acta Physiol. Scand. 107 (1979) 319–325.

[56] A. Eberstein, J. Goodgold, Slow and fast twitch fibers in human skeletal muscle, Am. J. Physiol.-Leg. Content 215 (1968) 535–541.

[57] M. Nikolić, D. Malnar-Dragojević, D. Bobinac, S. Bajek, R. Jerković, T. Šoić-Vranić, Age-related skeletal muscle atrophy in humans: an immunohistochemical and morphometric study, Coll. Antropologicum 25 (2001) 545–553.

[58] F. Eusebi, R. Miledi, T. Takahashi, Calcium transients in mammalian muscles, Nature 284 (1980) 560–561.

[59] L.C. Rome, C. Cook, D.A. Syme, M.A. Connaughton, M. Ashley-Ross, A. Klimov, B. Tikunov, Y.E. Goldman, Trading force for speed: why superfast crossbridge kinetics leads to superlow forces, Proc. Natl. Acad. Sci. 96 (1999) 5826–5831.

[60] BodyParts3D, Copyright 2008 life science integrated database center licensed by cc display-inheritance 2.1 japan, 2021, URL http://lifesciencedb.jp/bp3d/.

[61] N. Mitsuhashi, K. Fujieda, T. Tamura, S. Kawamoto, T. Takagi, K. Okubo, Bodyparts3d: 3d structure database for anatomical concepts, Nucleic Acids Res. 37 (2009) D782–D785.

[62] H. Axer, D.G.v. Keyserlingk, A. Prescher, Collagen fibers in linea alba and rectus sheaths: I. general scheme and morphological aspects, J. Surg. Res. 96 (2001) 127–134.

[63] S. Little, The Cat-E-Book: Clinical Medicine and Management, Elsevier Health Sciences, 2011.

[64] R.L. Drake, H. Gray, W. Vogl, A.W. Mitchell, Gray's Anatomy for Students, Elsevier Health Sciences TW, 2018.

[65] M.Á. Ariza-Gracia, J. Zurita, D.P. Piñero, B. Calvo, J.F. Rodriguez-Matas, Automatized patient-specific methodology for numerical determination of biomechanical corneal response, Ann. Biomed. Eng. 44 (2016) 1753–1772.

[66] B. De Keulenaer, J. De Waele, B. Powell, M. Malbrain, What is normal intra-abdominal pressure and how is it affected by positioning, body mass and positive end-expiratory pressure? Intensive Care Med. 35 (2009) 969–976.

[67] P. Neumann, V. Gill, Pelvic floor and abdominal muscle interaction: EMG activity and intra-abdominal pressure, Int. Urogynecol. J. 13 (2002) 125–132.

[68] M. Malbrain, N. Van Mieghem, W. Verbrugghe, R. Daelemans, R. Lins, Effects of different body positions on intra-abdominal pressure and dynamic respiratory compliance, in: Critical Care, Springer, 2003, p. 1.

[69] P. Martin-Du, R. Benoit, L. Girardier, The role of body position and gravity in the symptoms and treatment of various medical diseases, Swiss Med. Wkly. 134 (2004).

[70] H. Sugerman, A. Windsor, M. Bessos, L. Wolfe, Intra-abdominal pressure, sagittal abdominal diameter and obesity comorbidity, J. Int. Med. 241 (1997) 71–79.

[71] K. Szepietowska, I. Lubowiecka, B. Magnain, E. Florentin, Modelling of abdominal wall under uncertainty of material properties, in: International Symposium on Computer Methods in Biomechanics and Biomedical Engineering, Springer, 2019, pp. 305–316.

[72] B. Fereidoonnezhad, R. Naghdabadi, S. Sohrabpour, G. Holzapfel, A mechanobiological model for damage-induced growth in arterial tissue with application to in-stent restenosis, J. Mech. Phys. Solids 101 (2017) 311–327.